50 μm pixel pitch wafer-scale CMOS active pixel sensor x-ray detector for digital breast tomosynthesis

C Zhao[1], A C Konstantinidis[2,3], Y Zheng[2], T Anaxagoras[4], R D Speller[2] and J Kanicki[1]

[1] Solid-State Electronics Laboratory, Department of Electrical Engineering and Computer Science, University of Michigan, Ann Arbor, MI 48105, USA

[2] Department of Medical Physics and Biomedical Engineering, University College London, London WC1E 6BT, UK

[3] Diagnostic Radiology and Radiation Protection, Christie Medical Physics and Engineering, The Christie NHS Foundation Trust, Manchester M20 4BX, UK

[4] ISDI Ltd (Image Sensor Design and Innovation), Oxford OX4 1YZ, UK

E-mail: kanicki@eecs.umich.edu

CrossMark

Abstract

Wafer-scale CMOS active pixel sensors (APSs) have been developed recently for x-ray imaging applications. The small pixel pitch and low noise are very promising properties for medical imaging applications such as digital breast tomosynthesis (DBT). In this work, we evaluated experimentally and through modeling the imaging properties of a 50 μm pixel pitch CMOS APS x-ray detector named DynAMITe (Dynamic Range Adjustable for Medical Imaging Technology). A modified cascaded system model was developed for CMOS APS x-ray detectors by taking into account the device nonlinear signal and noise properties. The imaging properties such as modulation transfer function (MTF), noise power spectrum (NPS), and detective quantum efficiency (DQE) were extracted from both measurements and the nonlinear cascaded system analysis. The results show that the DynAMITe x-ray detector achieves a high spatial resolution of $10\,\text{mm}^{-1}$ and a DQE of around 0.5 at spatial frequencies $<1\,\text{mm}^{-1}$. In addition, the modeling results were used to calculate the image signal-to-noise ratio (SNR_i) of microcalcifications at various mean glandular dose (MGD). For an average breast (5 cm thickness, 50% glandular fraction), 165 μm microcalcifications can be distinguished at a MGD of 27% lower than the clinical value (~1.3 mGy). To detect 100 μm microcalcifications, further optimizations of the CMOS APS x-ray detector, image aquisition geometry and image reconstruction techniques should be considered.

(Some figures may appear in colour only in the online journal)

1. Introduction

Recently, x-ray imagers based on complementary metal-oxide-semiconductor (CMOS) active pixels sensor (APS) have been considered as an alternative to amorphous silicon (a-Si:H) passive pixel sensor (PPS) x-ray detectors in bio-medical imaging applications. CMOS APS detectors overcome the drawbacks of conventional detectors by using a pixel amplifier that effectively reduces the noise floor (Fossum 1995, El Gamal and Eltoukhy 2005). During the past few years, large area CMOS APS x-ray imagers with small pixel pitches ranging from 40 to 75 μm, low electronic noise of 50–165 e$^-$, dynamic range of 63–69 dB, fast frame rate of 20–30 fps have been developed (Bohndiek *et al* 2009, Konstantinidis *et al* 2013, Esposito *et al* 2011, 2014). Specifically, the 2D projection image quality of a CMOS APS x-ray imager with a 75 μm pixel pitch (Dexela 2923 MAM) has been intensively evaluated for breast imaging applications such as mammography and digital breast tomosynthesis (DBT) (Choi *et al* 2012, Konstantinidis *et al* 2012a, 2013, Patel *et al* 2012, Zhao *et al* 2015). Naday *et al* (2010) and Park *et al* (2014) also evaluated the DBT reconstructed images. As early indicators of breast cancer, detection of microcalcifications in sizes below 200 μm is critical but challenging for radiologists (Wheeler *et al* 2006). It was shown that experimentally important microcalcifications with 165 μm diameters could be resolved using the Dexela 2923 MAM x-ray detector with a mean glandular dose (MGD) of 2 mGy (Park *et al* 2014). However, to distinguish smaller microcalcifications such as 100 μm in size (Nyquist limit of 50 μm pixel pitch detectors), detectors with a pixel pitch of 50 μm or smaller and low electronic noise are needed.

Detector temporal performance such as lag and ghosting may cause image artifacts during the relative fast image acqulisition process of DBT. Lag is the residual image charge generated in previous exposed frames that remains in electronics in subsequent frames as offset charge, while ghosting is associated with the change in x-ray sensitivity induced by x-ray exposure (Zhao and Zhao 2008). For example, for conventional amorphous selenium (a-Se) based x-ray imagers, both lag and ghosting are caused by the charge trapping, ionization and recombination mechanisms with the subgap bulk and interface trap states of a-Se. Zhao and Zhao (2008) have reported 4–5% image lag and ghosting using an a-Se PPS-based DBT system. Unlike amorphous materials, the crystalline nature of CMOS APS x-ray detectors limits the bulk and interface traps of crystalline silicon (c-Si) to much lower values. As the result, a negligible image lag of <0.1% was reported (Zentai 2011). The ghosting is also expected to be minimal, which would not degrade the image. Therefore, CMOS APS x-ray detectors appear to be very promising for medical imaging technologies requiring fast frame rates (>5 fps), such as DBT.

The Multidimensional Integrated Intelligent Imaging (MI-3) Plus consortium has developed a novel 50 μm pixel pitch CMOS APS x-ray detector (Dynamic Range Adjustable for Medical Imaging Technology), named DynAMITe. Technical details on this detector will be discussed in section 2.1. Fundamental electro-optical properties of the DynAMITe x-ray detector were previously investigated (Esposito *et al* 2011, 2014). Konstantinidis *et al* (2012b) show that a high contrast-to-noise ratio (CNR) and acceptable contrast-detail performance for mammography application can be achieved using the DynAMITe x-ray detector. However, the x-ray imaging performance of such a high resolution x-ray detector has not been evaluated for the low dose DBT application.

To investigate detector key parameters such as modulation transfer function (MTF), noise power spectrum (NPS) and detective quantum efficiency (DQE), cascaded system analysis is a very useful tool (Siewerdsen *et al* 1997, Cunningham and Shaw 1999, Antonuk *et al* 2000, El-Mohri *et al* 2007). In such analysis, it is assumed that the signal and noise propagations are linear, which is valid for PPS based detectors. However, for CMOS APS x-ray detectors, the detector performance is affected by the signal and noise nonlinearity (Bohndiek *et al* 2008). Therefore, the cascaded linear system analysis has to be modified to address the nonlinearity issue for CMOS APS x-ray detectors.

In this work, the imaging properties (MTF, NPS and DQE) of the DynAMITe x-ray detector were characterized. We also modified the cascaded system model previously developed for CMOS APS x-ray detector (Zhao *et al* 2015) by integrating the detector nonlinear properties. Both the projection image quality (MTF, NPS and DQE) and the detector electrical properties (such as mean signal, noise, full well capacity (FW) and DR) were simulated using the revised model. As one of the indicators of breast cancer, it is of vital importance to distinguish small size microcalcifications in the reconstructed image. The image contrast of microcalcifications within an equivalent reconstructed breast slice of 1 mm thickness was evaluated by the breast image signal-to-noise ratio (SNR_i). Both the object contrast and detector performance extracted from experimental and cascaded system analysis results were integrated into the SNR_i calculation. At the same time, the mean glandular dose (MGD) was calculated using the method described in Sechopoulos *et al* (2007). Finally, SNR_i for 100 (Nyquist limit for DynAMITe SP detector) and 165 μm microcalcifications was extracted at various MGDs.

2. Materials and methods

2.1. The DynAMITe SP detector

The wafer scale (12.8×13.1 cm^2) DynAMITe CMOS APS x-ray detector was fabricated using the standard 0.35 μm CMOS technology (Scheffer 2007). Since the detector is two-side buttable, a 2×2 tiling of sub-detectors can cover a large area of 25.6×26.2 cm^2 suitable for DBT application (Esposito *et al* 2011).

The studied DynAMITe detector is dynamic range (DR) adjustable and can operate in either (a) high DR, full pixel mode (P mode, 100 μm pixel pitch), or (b) a high resolution, subpixel mode (SP mode, 50 μm pixel pitch). This is realized by activating either a pixel photodiode (P diode) in a 100×100 μm^2 full pixel area or a subpixel photodiode (SP diodes) in a 50×50 μm^2 subpixel area (Esposito *et al* 2011). The characteristics of DynAMITe P and SP modes are summarized in table 1 (Esposito *et al* 2011, 2014).

The switch between P and SP modes is not dynamic, i.e. either P or SP mode can be selected before an x-ray exposure. This will allow to switch between 100 and 50 μm pixel pitch. The SP mode achieves a small pixel pitch of 50 μm, large conversion gain of around 0.02 DN/e$^-$, low σ_R of around 150 e$^-$ and frame rate of 30 fps (Esposito *et al* 2011, 2014). These properties make the SP mode very promising for low dose applications such as DBT. Although not being characterized here, the existence of P mode offers the detector a possibility of being used to achieve high DR (68 dB) and fast frame rate (90 fps), that could be required for applications such as x-ray diffraction measurements (Konstantinidis *et al* 2012c).

In this work, we focus exclusively on the DynAMITe detector working in the SP mode with a pixel pitch of 50 μm. A 150 μm thick cesium iodide (CsI:Tl) scintillator with fiber optic plate (FOP) was integrated on top of the DynAMITe sensor.

Figure 1(a) shows a top view schematic representation of a CMOS APS x-ray detector. The entire pixel area consists of a photodiode active area and an area containing all the electronics

Table 1. Parameters and characteristics of DynAMITe P and SP cameras.

	P mode	SP mode
Pixel pitch (μm)	100	50
Pixel resolution	1280×1312	2560×2624
Full well capacity (e$^-$)	$\sim 1.9 \times 10^6$	$\sim 2.8 \times 10^5$
Conversion gain (DN/e$^-$)	3.4×10^{-3}	0.02
Read noise (e$^-$)	780	~ 150
Dynamic range	~ 2435, (68 dB)	~ 1867, (65 dB)
External quantum efficiency (%)	54	64
Pixel fill factor	0.7	0.7
Maximum full frame rate (fps)	90	30

such as transistors and bias lines. For DynAMITe SP detector, the pixel pitch (a_{pix}) is 50 μm giving a total pixel area of 2500 μm^2, while the fill factor ($FF = 0.7$) is the ratio of photodiode active area (1750 μm^2) to the total pixel area. In the cascaded system analysis, we assume that the photodiode active area is square. Hence, an effective photodiode pitch (a_{pd}) of 41.8 μm is defined such that a_{pd}^2 equals to the photodiode area.

The DynAMITe SP detector is based on the standard 3-trainsistor (3-T) CMOS APS technology. Figure 1(b) shows the circuit schematic of conventional 3-T CMOS APS with readout electronics (El Gamal and Eltoukhy 2005). RST, SF, RS and Bias represent the reset transistor, source follower, row select transistor in each pixel and bias transistor in the column circuit, respectively. The operation of CMOS APS is sequentially divided into three stages. (a) Reset stage: the RST is ON, and a constant bias (V_{RST}) is applied to the cathode of the photodiode. Electrons stored on the photodiode capacitance (C_{PD}) and the input pixel parasitic capacitance (C_{Par}) are removed. (b) Integration stage: RST and RS are OFF, optical photons converted from x-rays impinge the SP photodiode and create electron–hole (e–h) pairs. Generated e–h pairs are separated in the depletion region under the reverse bias. The input signal in electrons (d(e$^-$)) varies the voltage of the sensing node (gate voltage of SF, VG$_{SF}$). (c) Readout stage: RS and Bias are ON, while constant current is flowing through the bias transistor in the column circuit. Ideally, the voltage variance on the column capacitance (C_{COL}) follows VG$_{SF}$ (Salama and El Gamal 2003). CMOS APS coverts signal in electrons to voltages in the column circuit (d(V)). Finally, d(V) is amplified and converted to a digital number d(DN) as the output signal by an analog-to-digital converter (ADC).

The readout of DynAMITe detector is based on the rolling shutter method (Yadid-Pecht and Etienne-Cummings 2004): the rows of pixels are reset and read in a sequence. After the reset of row N, the readout process of row 1 begins. The integration time (around 0.2 s for DBT) is determined by the time gap between reset and readout for a row. Correlated double sampling (CDS) is not used for DynAMITe SP detector.

The DynAMITe detector has been designed according to the radiation hardness-by-design methodology. All the in-pixel transistors have been designed with source and drain physically enclosed using an enforced layout geometry (ELG) to reduce the edge leakage, which is generated in the transition area between thin gate oxide and the thick field oxide (Eid *et al* 2001, Lacoe 2008). The radiation hardness of this detector has been evaluated through x-ray radiation damage testing and shows a damage threshold of 204 Gy(Si), which is acceptable for medical imaging applications (Esposito *et al* 2012).
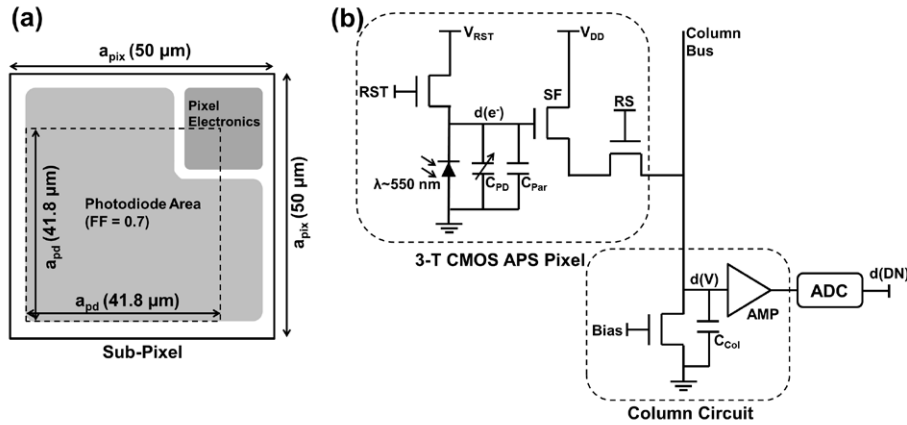
Figure 1. (a) Top view schematic representation of CMOS APS x-ray detector with 50 μm pixel pitch. a_{pix} and a_{pd} are the pixel pitch and effective photodiode pitch, respectively. (b) Circuit schematic of DynAMITe SP CMOS APS detector. RST, SF, RS and Bias represent the reset transistor, source follower, row select transistor and column bias transistor, respectively. C_{PD}, C_{Par} and C_{Col} are the photodiode capacitance, parasitic capacitance, and column capacitance, respectively. V_{RST} and V_{DD} are constant bias voltages.

2.2. Experimental

The DynAMITe SP x-ray detector was characterized by measuring the modulation transfer function (MTF), noise power spectrum (NPS) and detective quantum efficiency (DQE) at various x-ray exposure (also known as air kerma—K_a) levels. Figure 2 shows the experimental setup used for such measurements. A tungsten (W) anode x-ray tube with an inherent aluminum (Al) filtration of 1.4 mm was used as the x-ray source. An external filtration of 1.1 mm Al was added to reach a total filtration of 2.5 mm Al. According to the IEC standard for mammography (IEC 62220-1-2 2007), the tube voltage was set at 28 kVp and the half value layer (HVL) was measured as ~0.83 mm Al using the Raysafe Xi dosimeter, which contains Al filtration internally and calculates automatically the HVL. The DynAMITe SP x-ray detector was placed at 60.5 cm from the x-ray source. The source to detector distance is similar to those DBT systems in clinical use (~65 cm) (Sechopoulos 2013). In this experiment, both the x-ray source and detector were in stationary positions.

2.2.1. X-ray fluence. For a fixed x-ray spectrum, the mean x-ray fluence ($\overline{q_0}$), defined by the number of incident x-ray quanta per unit area, is proportional to the detector exposure in air kerma (K_a). The mean x-ray fluence per exposure ratio ($\overline{q_0}/K_a$) in x-rays mm^{-2} μGy^{-1} is described by (Boone 1998)

$$\overline{q_0}/K_a = \int_0^{E_{\max}} \Phi_{0,\text{norm}}(E)\left(\frac{q_0}{K_a}(E)\right)dE = \int_0^{E_{\max}} \Phi_{0,\text{norm}}(E)\frac{W \cdot Q}{(\mu_{en}(E)/\rho)_{\text{air}} \cdot E \cdot q \cdot 10^8}dE \qquad (1)$$

where $\Phi_{0,\text{norm}}$ is the normalized x-ray spectrum (sum up to unity), (q_0/K_a) is the x-ray fluence per exposure at each energy E, W is the air work function (33.97 eV), Q is the charge liberated in air by one Roentgen (R) (2.58×10^{-4} C kg^{-1} R^{-1}), q is the electron charge and $(\mu_{en}(E)/\rho)_{\text{air}}$ is the mass energy absorption coefficient of air. For our system,
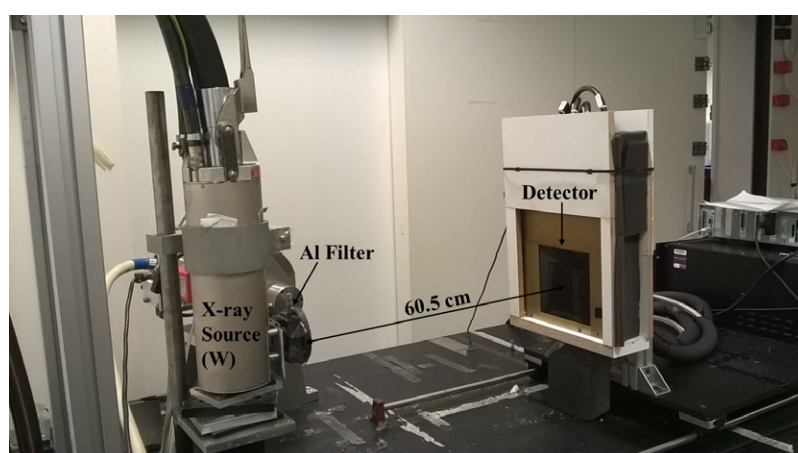
Figure 2. Experimental setup for detector MTF, NNPS and DQE measurements.

$\overline{q_0}/K_a = 7009$ x-rays mm^{-2} μGy^{-1}. This number was calculated using the SPEKTR software (Siewerdsen *et al* 2004) for the W/Al x-ray source with 28 kVp tube voltage used in this study. Briefly, this software simulates the normalized x-ray spectrum with the added filtration ($\Phi_{0,\text{norm}}$); then (q_0/K_a) at each energy E is calculated. Finally the $\overline{q_0}/K_a$ is calculated by integrating (q_0/K_a) over $\Phi_{0,\text{norm}}$. The HVL was also calculated by SPEKTR to be 0.824 mm Al, which is consistent with the measured value for the x-ray source used. By replacing the detector to a dosimeter (Raysafe Xi), K_a values for various exposure conditions were measured.

2.2.2. Modulation transfer function (MTF). The MTF measures the change in signal amplitude through an imaging system in the spatial frequency domain. The tilted edge technique was used to measure the MTF of DynAMITe SP detector (Samei *et al* 1998). An x-ray opaque, polished edge plate (W foil, 1 mm thick, 99.95% pure) was placed in front of the detector at a small tilted angle (1.5–3°) with respect to the detector rows and columns. A number of raw edge images ($N = 20$ to reduce the random noise) was captured when placing the edge horizontally and vertically. A standard gain and offset correction algorithm was applied to remove the fixed pattern noise (FPN) by capturing additional 10 frames of flat and dark images without the edge sample (Konstantinidis 2011). After that, a second order polynomial fit correction was applied to remove the low spatial frequency trends caused by the x-ray field non-uniformity (IEC 62220-1-2 2007, Konstantinidis 2011).

The corrected pixel values of several consecutive lines across the edge were used to generate the edge spread function (ESF) curves. These ESF curves were laterally shifted to the same position and combined (averaged) to reduce the statistical noise. The average oversampled ESF was differentiated to obtain the oversampled line spread function (LSF). Finally, a Fourier transform (FT) of the LSF gives the MTF in the spatial frequency domain corresponding to either spatial x or y direction (Konstantinidis *et al* 2012a). The process of MTF extraction is summarized by the following expression

$$\text{MTF}(u) = |\text{FT}\{\text{LSF}(x)\}| = \left| \text{FT}\left\{ \frac{\text{d}}{\text{d}x}[\text{ESF}(x)] \right\} \right| \tag{2}$$

2.2.3. Noise power spectrum (NPS). The NPS describes the change in signal variance through an imaging system in the spatial frequency domain. The NPS was measured from the flat field and dark images acquired in section 2.2.2. A subtraction algorithm was applied for gain and offset correction. The NPS was measured based on the IEC standard (IEC 62220-1-2 2007). First, overlapping regions of interest (ROI) of 256×256 pixels were selected from a central area (1280×1280 pixels) of the corrected image. Then a second order polynomial fit ($S(x, y)$) was performed to the corrected flat-field image ($I(x, y)$) to remove the low frequency (background) trends. The 2D NPS profile can be calculated from the sum of Fourier transforms of ($I(x, y) - S(x, y)$) for all the ROIs

$$\text{NPS}(u, v) = \frac{\Delta x \cdot \Delta y}{N_{\text{ROI}} \cdot N_x \cdot N_y} \sum_{i=1}^{M} |\text{FT}\,[I(x_i, y_i) - S(x_i, y_i)]\,|^2 \tag{3}$$

where Δx and Δy are the pixel pitches in x and y directions, N_{ROI} is the number of ROIs, N_x and N_y gives the number of rows and columns in each ROI ($N_x = N_y = 256$). We selected three frames of corrected images with 1280×1280 pixels each to realize more than four millions of individual pixels as required by the IEC 62220-1-2 (2007). In each frame, 9 by 9 ROIs (of 256×256 pixels each) were selected with a shift of 128 pixels (half-overlapping ROIs according to the IEC 62220-1-2 standard). Therefore, $N_{\text{ROI}} = 9 \times 9 \times 3 = 243$.

Data from seven rows and columns on both side of the zero spatial frequency (a total of 14 lines) was extracted and averaged, resulting in the horizontal and vertical 1D NPS. The 1D normalized NPS (NNPS) was calculated by $\text{NNPS}(u) = \text{NPS}(u) / d(\text{DN})^2$, where $d(\text{DN})$ is the mean large area output signal in digital number. The above steps were repeated to extract 1D NNPS for various x-ray exposure levels.

The mean signal $d(\text{DN})$ and mean variance $\sigma^2(\text{DN}^2)$ (i.e. the spatial mean of the temporal variance) were also experimentally determined from the flat field images captured for NNPS calculation using the following expressions (Pain and Hancock 2003, Bohndiek *et al* 2008)

$$d(\text{DN}) = \frac{1}{MN} \sum_{i,j} \overline{d_{i,j}}, \quad \text{where } \overline{d_{i,j}} = \frac{1}{L} \sum_{k} d_{i,j,k} \tag{4}$$

and

$$\sigma^2(\text{DN}^2) = \frac{1}{MN} \sum_{i,j} \overline{\sigma_{i,j}^2}, \quad \text{where } \overline{\sigma_{i,j}^2} = \frac{1}{L} \sum_{k} d_{i,j,k}^2 - (\overline{d_{i,j}})^2 \tag{5}$$

where M and N are the pixel numbers in x and y direction, L ($=10$) is the number of flat field images, $\overline{d_{i,j}}$ and $(\overline{\sigma_{i,j}})^2$ are the mean signal and variance at position (i, j) over L frames, respectively.

2.2.4. Detective quantum efficiency (DQE). DQE is the ratio between the square of output $(\text{SNR}_{\text{out}})^2$ and input signal-to-noise ratio $(\text{SNR}_{\text{in}})^2$. Since $(\text{SNR}_{\text{in}})^2$ is the x-ray fluence ($\overline{q_0}$) multiplied by the pixel area (a_{pix})^2, DQE indicates the dose efficiency. Based on experimental results in sections 2.2.1–2.2.3, the 1D DQE can be calculated by

$$\text{DQE}(u) = \frac{(\text{SNR}_{\text{out}})^2}{(\text{SNR}_{\text{in}})^2} = \frac{d(\text{DN})^2 \cdot \text{MTF}(u)}{\overline{q_0} \cdot \text{NPS}(u)} = \frac{\text{MTF}(u)}{\overline{q_0} \cdot \text{NNPS}(u)}. \tag{6}$$

The experimental results of MTF, NPS and DQE are shown in figures 4 and 5, respectively. These data are compared with simulated data obtained using cascaded system analysis to be discussed in section 2.3.

Table 2. Parameters used in the cascaded system model.

Parameter	Value	Description
$\overline{q}_0/K_a$	7009 x-rays mm^{-2} μGy^{-1}	Mean x-ray fluence/air kerma
$\overline{g}_1$	0.55	Mean x-ray absorption
$\overline{g}_2$	580	Scintillator mean quantum gain
I_S	0.87	Swank factor
ε_{g2}	85.7	Scintillator Poisson excess
H_3	0.29	Scintillator blurring fitting parameter
$\overline{g}_4$	0.44	FOP optical coupling efficiency
H_5	0.06	FOP blurring fitting parameter
$\overline{g}_6$	0.64	Photodiode EQE
FF	0.7	Pixel fill factor
a_{pix}	50 μm	Pixel pitch
a_{pd}	41.8 μm	Effective photodiode pitch
$g_{9,S}$	0.024−0.023 DN/e$^-$	Signal conversion gain of CMOS APS
$g_{9,N}$	0.025−0.022 DN/e$^-$	Noise conversion gain of CMOS APS
σ_R	145 e$^-$	Additive read noise

2.3. Cascaded system analysis

Cascaded system analysis was performed to evaluate the imaging performance of the 50 μm pixel pitch DynAMITe SP CMOS APS x-ray detector. The x-ray imaging process is divided into a series of gain and spreading stages (Siewerdsen *et al* 1997). For each stage, the propagations of signal and noise are assumed to be linear. However, this assumption is not valid for CMOS APS x-ray detectors (Bohndiek *et al* 2008). The signal and noise nonlinearity of CMOS APS needs to be included in the cascaded system analysis. In this work, a 9-stage nonlinear cascaded system was developed and used.

Stage 0*: Incident x-ray quanta.* $\overline{q}_0/K_a$ for the 28 kVp W/Al x-ray source used in this work is 7009 x-rays mm^{-2} μGy^{-1}. Therefore, the x-ray fluence ($\overline{q}_0$) in x-rays/mm^2 is simply given by ($\overline{q}_0/K_a$) $\times$ K_a (table 2).

Stage 1*: X-ray absorption by CsI:Tl scintillator.* The first gain stage of the system describes the mean x-ray absorption by the scintillator ($\overline{g}_1$). For cascaded system, $\overline{g}_1$ is generally determined by the quantum detection efficiency (QDE), representing the mean number of absorbed x-rays per incident x-ray quanta (Siewerdsen *et al* 1997, Vedantham *et al* 2004). However, as the scintillator is energy integrator rather than photon counter (Van Metter *et al* 2000), the energy absorption efficiency (EAE), defined by the mean energy absorbed per incident unit of energy, gives a better estimation of the maximum detectability of the system for x-ray energies below the K-absorption edge of iodine at 33.2 keV (Konstantinidis *et al* 2013). Hence, in this work, we used EAE to calculate the x-ray absorption by scintillator. $\overline{g}_1$ is given by

$$\overline{g}_1 = \text{EAE} = \frac{\int_0^{E_{max}} \Phi_0(E) \cdot T_0(E) \cdot E \cdot \left(\frac{\mu_{en}(E)}{\mu(E)}\right) \cdot (1 - e^{-\mu(E)t}) \cdot dE}{\int_0^{E_{max}} \Phi_0(E) \cdot E \cdot dE} \tag{7}$$

where $\Phi_0(E)$ is the x-ray energy spectrum as a function of x-ray photon energy (E), $T_0(E)$ is the transmission (~0.85) of the scintillator protection layer, t is the scintillator thickness (150 μm), $\mu(E)$ and $\mu_{en}(E)$ are the linear attenuation and energy absorption coefficients of

the scintillator, respectively (Van Metter *et al* 2000). The calculated $\overline{g_1}$ for our system by equation (7) is 0.55 (table 2).

Stage 2*: Optical photon generation and emission in scintillator.* This gain stage combines the optical photon generation and emission. The optical yield (η_{opt}) of scintillator in photons/keV gives the number of optical photons generated per absorbed x-ray quanta per unit energy. Reported η_{opt} for CsI:Tl scintillator ranges from 55 to 66 photons/keV (Holl *et al* 1988, Nikl 2006). In our cascaded system analysis, η_{opt} of 58 photons/keV was used (table 2) according to Vedantham *et al* (2004).

The fraction of generated photons that can escape from the scintillator ($\eta_{\text{esc}}(z)$) is associated with the vertical distance z to the bottom interface with FOP (Hillen *et al* 1991). The light output in number of escaped optical photons per absorbed x-ray quanta of energy E at position z is given by $g_2(E, z) = \eta_{\text{opt}} \times E \times \eta_{\text{esc}}(z)$. The mean light output (number of optical photons) per absorbed x-ray by a scintillator with thickness t is given by (Vedantham *et al* 2004)

$$\overline{g_2} = \frac{\int_0^{E_{\max}} \int_{z=t}^0 \Phi_0(E)(e^{-\mu(E)(t-z)})(1 - e^{-\mu(E)\mathrm{d}z})g_2(E, z)\mathrm{d}z\mathrm{d}E}{\int_0^{E_{\max}} \Phi_0(E)T_0(E)(1 - e^{-\mu(E)t})\mathrm{d}E}. \tag{8}$$

The calculated $\overline{g_2}$ is 580 over the entire x-ray spectrum ($E_{\max} = 28$ keV) for scintillator thickness t of 150 μm. The Poisson excess (ε_{g2}) describes the gain variance of $\overline{g_2}$, which is given by

$$\varepsilon_{g2} = \overline{g_2}\left(\frac{1}{I_S} - 1\right) - 1 \tag{9}$$

where I_S is the Swank factor quantifying the noise associated with x-ray to photon conversion process (Zhao *et al* 2004, El-Mohri *et al* 2007). Taking I_S of 0.87, ε_{g2} of 85.7 is obtained (table 2).

Stage 3*: Scintillator scattering.* The lateral scattering of optical photons in the scintillator can introduce optical cross-coupling between imager pixels leading to image blur and degradation of image quality. This is the first blurring stage that spatial frequency is included in the cascaded system. The scintillator scattering can be approximated by a Lorentzian fit to the experimental data (Siewerdsen *et al* 1997)

$$T_3(u, v) \approx (1 + H_3(u^2 + v^2))^{-1} \tag{10}$$

where H_3 (~0.29) is obtained by fitting the experimental MTF data (figure 4) with given $T_5(u,v)$ (Jain *et al* 2011) and $T_7(u,v)$ (equation (15)) to be discussed later, u and v are the spatial frequencies in x and y direction, respectively. The fitted $T_3(u,v)$ curve is close to the extracted curve for a 150 μm (used in this study) high light output CsI:Tl scintillator on a 3 mm thick FOP (El-Mohri *et al* 2007).

It is known that CsI:Tl forms needle-shaped crystal columns that prevent the optical cross-coupling. Sharma *et al* (2012) studied the impacts of CsI:Tl structure and optical properties on the scintillator MTF (T_3) through Monte Carlo simulations. It was observed that the scintillator MTF would increase with a larger bulk absorption coefficient, reduced surface roughness, smaller inter-column distance and suppressed columnar wall crossover in the first monolayer of the scintillator in contact with the FOP. In this work, all these effects are included in H_3, i.e. a smaller H_3 value will lead to an improved $T_3(u,v)$. Accurate modeling of the optical behavior of CsI:Tl is beyond the scope of this paper. Also better microscopic knowledge of underlying scintillator physics and optical properties will not affect the conclusion of this work.

Stage 4*: Optical coupling of the fiber optic plate*. The CsI:Tl scintillator is attached to the CMOS image sensor by the FOP. The optical photons that escape from the scintillator impinge the FOP. The optical coupling efficiency ($\overline{g_4}$) defined by the fraction of photons transmitted through the FOP is given by (Hejazi and Trauernchit 1997)

$$\overline{g_4} = NA^2 T_F (1 - L_R) F_C \tag{11}$$

where NA (~1) is the numerical aperture of a fiber optic, T_F (~0.65) is the transmittance of fiber optic core, L_R (~0.1) is the Fresnel reflection optical loss at the surface and F_C (0.75) is the fill factor of the fiber optic core (Hejazi and Trauernichit 1997, Jain *et al* 2011). Calculated $\overline{g_4}$ of 0.44 was used for the cascaded system analysis (table 2).

Taking the above stages into consideration, the NPS at stage 4 is given by (Siewerdsen *et al* 1997)

$$S_4(u, v) = \overline{q_0 g_1 g_2 g_4}[1 + \overline{g_4}(\overline{g_2} + \varepsilon_{g2})T_3^2(u, v)]. \tag{12}$$

Stage 5*: Image blurring by the fiber optic plate*. In addition to the scintillator, the FOP also blurs the image (Jain *et al* 2011). Equation (10) can be also used to model the FOP blurring ($T_5(u,v)$) by changing H_3–H_5 of around 0.06 to fit the data from Jain *et al* 2011. Since the FOP blurring is a stochastic spreading stage (Cunningham and Shaw 1999), the NPS at stage 5 can be written as

$$S_5(u, v) = (S_4(u, v) - \overline{q_0 g_1 g_2 g_4})T_5^2(u, v) + \overline{q_0 g_1 g_2 g_4} = \overline{q_0 g_1 g_2 g_4}[1 + \overline{g_4}(\overline{g_2} + \varepsilon_{g2})T_3^2(u, v)T_5^2(u, v)]. \tag{13}$$

Stage 6*: Photon absorption and electron generation by photodiode*. The optical photons that escape the FOP are absorbed by the c-Si photodiode. Photo-induced carriers are generated in the depletion region and electrons are captured by the N^+ well. The gain of this stage ($\overline{g_6}$) represents the number of electrons collected per incident photon, i.e. the external quantum efficiency (EQE) of photodiode. $\overline{g_6}$ (EQE) of 0.64 was reported (Esposito *et al* 2011). The NPS at this stage is

$$S_6(u, v) = S_5(u, v)\overline{g_6}^2 + \overline{q_0 g_1 g_2 g_4 g_6}(1 - \overline{g_6}) \tag{14}$$

Stage 7*: Pixel presampling and blurring*. The imager pixel blurring associated with the photodiode active area is expressed as (Siewerdsen *et al* 1997, Tward and Siewerdsen 2008)

$$T_7(u, v) = \left|\text{sinc}(\pi a_{pd} u) \cdot \text{sinc}(\pi a_{pd} v)\right| \tag{15}$$

where a_{pd} is the effective pitch of the photodiode as shown in figure 1(a) (Cunningham 1997). We assume that the photodiode active area is square. A smaller a_{pd} will lead to a greater $T_7(u,v)$ and thus MTF(u,v) at high spatial frequencies. Therefore, a high resolution detector (e.g. 50 μm pixel pitch) is need for DBT to distinguish fine details (such as microcalcifications) associated with high spatial frequencies (>5 lp mm^{-1}).

As this spreading stage is deterministic, the NPS of stage 7 is given by

$$S_7(u, v) = a_{pd}^4 S_6(u, v) T_7(u, v) \tag{16}$$

Up to this stage, all the spreading stages have been described. The system presampling MTF can be written as

$$\text{MTF}(u, v) = T_3(u, v) T_5(u, v) T_7(u, v) \tag{17}$$

$d(e^-) = (a_{pd})^2 \overline{q_0 g_1 g_2 g_4 g_6}$ gives the electrical signal in electrons on the sensing node (gate of SF).

Stage 8*: NPS aliasing*. The limiting spatial frequency (Nyquist frequency, f_{Nyq}) is given by $1/(2a_{pix})$ because of aliasing. For the DynAMITe SP detector with $a_{pix} = 50$ μm, $f_{Nyq} = 10\,\text{mm}^{-1}$. This stage represents the NPS aliasing of the detector. The NPS after aliasing is given by (Antonuk *et al* 2000, El-Mohri *et al* 2007, Tward and Siewerdsen 2008)

$$S_8(u, v) = S_7(u, v) * * III_8(u, v) = \sum_{m,n=-\infty}^{+\infty} S_7\left(u - \frac{m}{a_{pix}}, v - \frac{n}{a_{pix}}\right) \tag{18}$$

where m and n are integers, and $III_8(u,v)$ is a Fourier transform of the sampling grid (comb function) (Antonuk *et al* 2000).

Stage 9*: CMOS APS conversion gain and read noise*. The last stage of the cascaded system describes the electron-to-DN conversion process and includes additional read noise for CMOS APS. The conversion gain (G) in DN/e$^-$ of CMOS APS is defined as the ratio between the variations in output (in DN) and input signals (in e$^-$). The mean-variance (MV) analysis method is widely used to extract G and σ_R for CMOS image sensors (Bohndiek *et al* 2008, Esposito *et al* 2011, Konstantinidis *et al* 2012a). The total variance of the digital signal (σ_S^2) as a function of output digital signal d(DN) is given by

$$\sigma_S^2(\text{DN}^2) = G(\text{DN/e}^-)d(\text{DN}) + \sigma_R^2(\text{DN}^2) \tag{19}$$

where the conversion gain G(DN/e$^-$) and the read noise σ_R(DN) can be extracted from the slope and intercept of the mean variance curve (mean variance ($\sigma_S^2/(\text{DN}^2)$) vs mean signal (d(DN))). Note that this method is commonly used with the optical illumination, thus the detector is tested using a light source without scintillator. The input referred read noise in electrons (at N$^+$-well of photodiode) is simply $\sigma_R(\text{e}^-) = \sigma_R(\text{DN})/G(\text{DN/e}^-)$. For DynAMITe SP, G of ~0.02 DN/e$^-$ and $\sigma_R(\text{e}^-)$ of ~150 e$^-$ was extracted from previous work (Esposito *et al* 2011).

The above analysis only holds for linear signal and noise responses. Cascaded system analysis also requires that the x-ray imaging system has a linear response (Siewerdsen *et al* 1997). However, since CMOS APS detectors are always nonlinear, the extracted G(DN/e$^-$) and cascaded system analysis could result in error (Bohndiek *et al* 2008). This issue can be addressed by applying the nonlinear compensation method (Bohndiek *et al* 2008, Janesick *et al* 2009). A signal conversion gain (S(e$^-$/DN)) and a noise conversion gain (N(e$^-$/DN)) are extracted and adapted to the cascaded system analysis separately. Both S(e$^-$/DN) and N(e$^-$/DN) are signal-dependent. The NPS of the final stage is given by

$$\text{NPS}(u, v) = (S_8(u, v) + a_{pix}^2 \sigma_R^2)g_{9,N}^2 + (a_{pd}^4 \overline{q_0 g_1 g_2 g_4 g_6})\sigma_{g9,N}^2 \tag{20}$$

where $g_{9,N}(\text{DN/e}^-) = 1/N(\text{e}^-/\text{DN})$ is the noise conversion gain in DN/e$^-$ and $(\sigma_{g9,N})^2$ is the variance of $g_{9,N}$. For DynAMITe SP detector, $\sigma_{g9,N} = 0.35 \times g_{9,N}$ was obtained from previous work (Esposito *et al* 2014). σ_R of 145 e$^-$ is used for the simulation (table 2).

The mean variance can be extracted by the following integral (Tward and Siewerdsen 2008)

$$\sigma^2(\text{DN}^2) = \int\int_{u,v=-f_{Nyq}}^{f_{Nyq}} \text{NPS}(u, v)\text{d}u\text{d}v. \tag{21}$$

Note that $\sigma^2(\text{DN}^2)$ is the mean variance of signal under x-ray exposure, while $\sigma_S^2(\text{DN}^2)$ in equation (19) is the mean variance of signal under light illumination.

The final stage digital output in DN is given by

$$d(\text{DN}) = a_{pd}^2 \overline{q_0 g_1 g_2 g_4 g_6} g_{9,S} \tag{22}$$

where $g_{9,S}(DN/e^-) = 1/S(e^-/DN)$ is the signal conversion gain in DN/e⁻. The normalized noise power spectrum, NNPS(u,v), is given by NPS(u,v)/d^2(DN). Hence, the DQE is calculated by equation (6).

At the same time, the detector output SNR (SNR_d) in decibel (dB) is given by

$$\mathrm{SNR}_d(\mathrm{dB}) = 20\log\left(\frac{d(\mathrm{DN})}{\sigma(\mathrm{DN})}\right). \tag{23}$$

All the parameters extracted and used for the cascaded system analysis are summarized in table 2.

2.4. Signal and noise non-linearity

The signal nonlinearity originates from both the sensitivity (V/e⁻) nonlinearity at the sensing node and the voltage gain (V/V) nonlinearity (Janesick *et al* 2009). In this work, we neglected the V/V nonlinearity and only considered the V/e⁻ nonlinearity.

Since the photodiode capacitance (C_{PD}) varies under different reverse bias, V/e⁻ nonlinearity is expected. C_{PD} at a low signal ($d(e^-) = (a_{pd})^2 \overline{q_0 g_1 g_2 g_4 g_6} \sim 0$) is expressed as

$$C_{PD}(0) = a_{pd}^2 \left(\frac{2}{q\varepsilon_S N_A}(V_{bi} + V_{RST})\right)^{-1/2} \tag{24}$$

where ε_S is the dielectric constant of silicon, N_A is the doping concentration of the P⁻ epitaxial layer, V_{bi} is the built-in voltage of the p⁻-n⁺ junction, V_{RST} is the reset voltage. As shown in figure 1(b), the total capacitance at the input sensing node (C_{IN}) is the sum of C_{PD} and a constant parasitic capacitance (C_{Par}). Therefore, C_{IN} as a function of $d(e^-)$ can be estimated by

$$C_{IN}(d(e^-)) = C_{PD}(d(e^-)) + C_{Par} = a_{pd}^2 \left(\frac{2}{q\varepsilon_S N_A}\left(V_{bi} + V_{RST} - \frac{qd(e^-)}{C_{PD}(0)}\right)\right)^{-1/2} + C_{Par}. \tag{25}$$

It is well known that the conversion gain of CMOS image sensors is proportional to $q/C_{IN}(d(e^-))$. Thus the signal conversion gain $g_{9,S}(DN/e^-)$ in section 2.3 was extracted by $g_{9,S}(0) \times (C_{IN}(0) / C_{IN}(d(e^-)))$, where $g_{9,S}(0)$ (~ 0.24 DN/e⁻) was obtained using the MV analysis at very low signal region. In the analysis described in this work, $C_{PD}(0)$ of ~12 fF and C_{Par} of ~28 fF were used.

The method to extract the noise gain is described as follows (Bohndiek *et al* 2008, Janesick *et al* 2009): It is assumed that the signal and noise gain are equal at low optical illumination or low x-ray exposure, i.e. $S(e^-/DN) = N(e^-/DN)$. We extract the conversion gain at low illumination $S_1(e^-/DN)$ by linear fitting of the MV curve (Esposito *et al* 2011). The signal at the sensing node at the lowest exposure level is $d_1(e^-) = d_1(DN) \times S_1(e^-/DN)$. Since signal nonlinearity only occurs at the CMOS APS level, linear response is expected for $d(e^-)$. Hence, the electron signal at x-ray exposure level n ($d_n(e^-)$) is proportional to the x-ray exposure, i.e. $d_n(e^-) = d_1(e^-) \times (K_{a,n}/K_{a,1})$. The noise gain is given by $N_n(e^-/DN) = d_n(e^-)^{1/2}/\sigma_{shot,n}(DN)$, where $\sigma_{shot,n}(DN)$ is the corresponding optical shot noise for the x-ray exposure level n. The variance $(\sigma_{shot,n}(DN))^2$ can be obtained from the MV graph (Esposito *et al* 2011) by $(\sigma_{S,n}(DN))^2 - (\sigma_R(DN))^2$ based on equation (19).

We can also get the signal gain $S_n(e^-/DN)$ by using $d_n(e^-)/d_n(DN)$. The $g_{9,S}(DN/e^-)$ (=$1/S(e^-/DN)$) extracted using this method (~0.24 DN/e⁻) is similar to the values extracted using $q/C_{IN}(d(e^-))$. Figure 3 shows the extracted $S(e^-/DN)$ and $N(e^-/DN)$ at detector exposure up to 127 μGy. It can be seen that the noise gain $N(e^-/DN)$ increases at
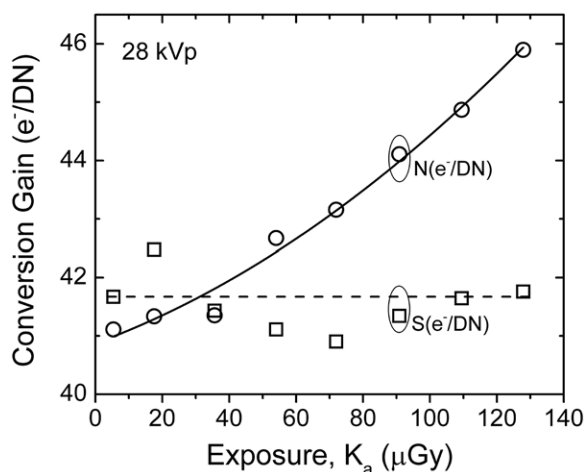
Figure 3. Extracted CMOS APS signal $S(e^-/DN)$ and noise $N(e^-/DN)$ conversion gains (symbols) at detector air kerma up to 127 μGy. A second order polynomial is used to fit $N(e^-/DN)$ (solid line).

large x-ray exposure, while the signal gain $S(e^-/DN)$ remains approximately constant. A second order polynomial fit was applied for $N(e^-/DN)$ and $g_{9,N}(DN/e^-)$ was calculated as $1/N(e^-/DN)$. At large x-ray exposure, we have $g_{9,N}(DN/e^-) < g_{9,S}(DN/e^-)$, i.e. a lower output noise but a larger output signal. As a result, the signal-to-noise property should be enhanced and an improved maximum DQE is expected. The impact of signal and noise nonlinearity on imaging performance will be discussed in section 3.1.

3. Results and discussion

3.1. Imaging performance of DynAMITe SP detector

Figure 4 illustrates the experimental and simulated MTF curves up to $f_{Nyq} = 10\,mm^{-1}$ at x-ray tube voltage 28 kVp. Simulated MTFs representing the scintillator spreading ($T_3(u,v)$), FOP blurring ($T_5(u,v)$) and pixel sampling ($T_7(u,v)$) based on cascaded system analysis are also shown. Thanks to the pixel pitch of 50 μm, the f_{Nyq} achieved for DynAMITe SP detector is doubled in comparison to current clinical systems with pixel pitches of ~100 μm (f_{Nyq} of ~ 5 mm^{-1}) (Sechopoulos 2013). It can be seen that for such a high resolution x-ray imager, the limiting factor for spatial resolution (i.e. system presampling MTF) is the scintillator scattering rather than the pixel blurring. Therefore, from this work, we can conclude that for imagers with higher resolution, the signal transfer property of CsI:Tl or any other scintillator needs to be improved. Specifically, the structural design (Cha *et al* 2008) and thickness of scintillator need to be optimized for a given imager application, which is outside the present study.

The measured and simulated (a) 1D NNPS and (b) DQE at a wide K_a range from 1.3 to 109.5 μGy are shown in figure 5. Signal and noise non-linearity was included. For typical DBT detector exposures ($K_a >17.6\,\mu$Gy), the DynAMITe SP x-ray detector achieves a DQE of >0.5 and ~0.1 at low spatial frequencies (<1 mm^{-1}) and $f_{Nyq} = 10\,mm^{-1}$, respectively. The DQE at low spatial frequencies is comparable to a clinical DBT system (Bissonnette *et al* 2005), while the maximum spatial resolution (f_{Nyq}) is extended from ~5 to 10 mm^{-1}. The DQE at the $f_{Nyq} = 10\,mm^{-1}$ does not vanish, demonstrating that the studied imager is capable to distinguish microcalcifications in the dimension of 100 μm.
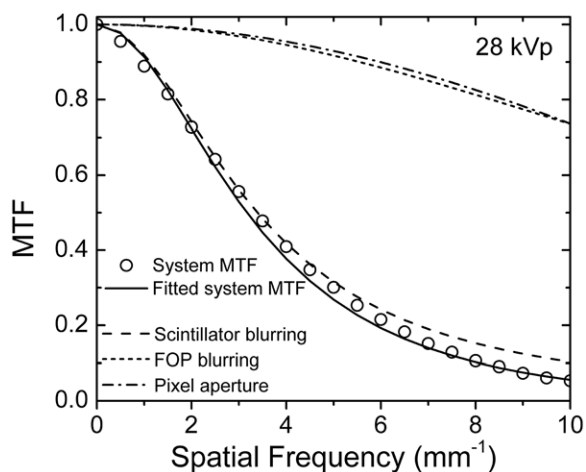
Figure 4. Experimental (circles) and simulated (solid line) system MTF. The stage MTFs associates with scintillator blurring, FOP blurring and pixel aperture are also shown (dash lines).
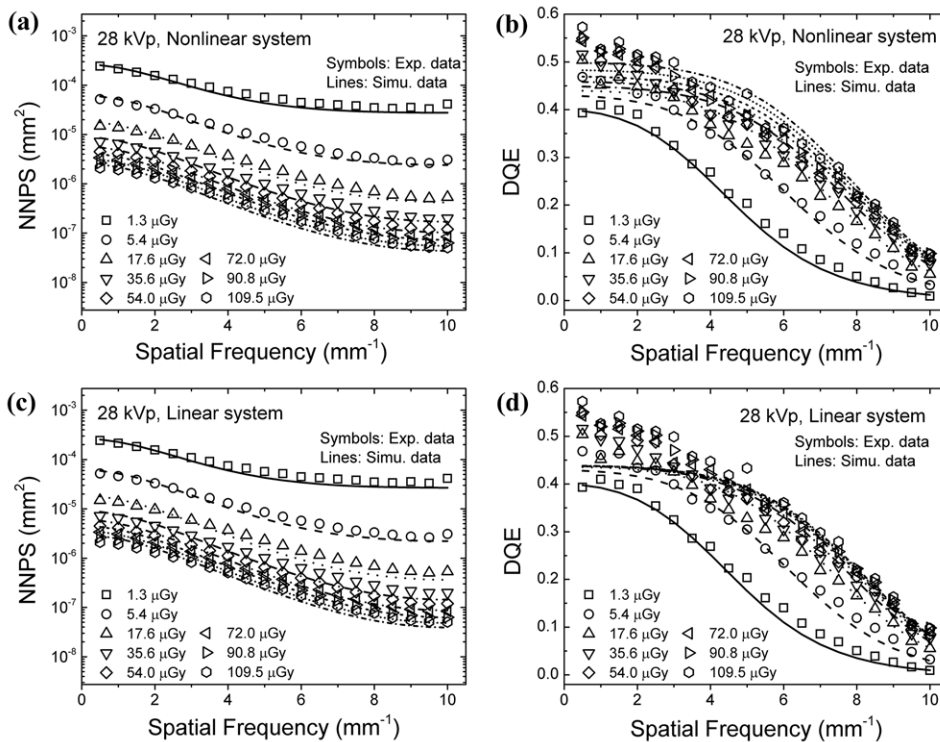

Figure 5. Experimental (symbols) and simulated (lines) (a) nonlinear system NNPS and (b) nonlinear system DQE for detector air kerma ranging from 1.3 to 109.5 μGy. For comparison purpose, (c) NNPS and (d) DQE data simulated using linear cascaded system analysis is also shown.

At low x-ray exposures ($K_a < 5.4\ \mu$Gy), the DQE drops especially in the high spatial frequency region ($>5\ \text{mm}^{-1}$). It was found that the drop in DQE at low exposure levels is due to the electronic noise because in these levels the detector system is not quantum-limited. However, the DQE reflects only the physical performance of the x-ray detectors instead of the image quality. The image quality at low dose is represented by the image signal-to-noise ratio that will be evaluated in section 3.3.

For comparison purpose, we also simulated the NNPS and DQE using linear cascaded system analysis. As shown in figures 5(c) and (d), if both the signal and noise are considered linear, the DQE at low spatial frequency saturates at a value (~0.45) smaller than the experimental results, when a high exposure ($>17.6\ \mu$Gy) is used. At $K_a = 109.5\ \mu$Gy and spatial frequency of 0.5 lp mm^{-1}, the NNPS and DQE differences between linear and nonlinear cascaded system analysis are 14% and 12%, respectively. Although not obvious in figure 5, the NNPS variation is nontrivial leading to clearly visible DQE drop at spatial frequencies close to zero. Hence, signal and noise non-linearity should be included in the cascaded system analysis (especially for higher K_a) to precisely describe the NNPS and DQE variations as a function of the spatial frequency.

Unlike the conventional PPS x-ray detectors (Antonuk *et al* 2000, El-Mohri *et al* 2007), in which the signal and noise response is linear, the DQE of DynAMITe SP CMOS APS x-ray imager does not saturate at high exposure values. Instead, the DQE increases with K_a for the entire spatial frequency range. This increase can be addressed by introducing the CMOS APS signal ($g_{9,S}(\text{DN/e}^-)$) and noise gains ($g_{9,N}(\text{DN/e}^-)$) to the cascaded system analysis. After the detector nonlinearity compensation being taken into account, both simulated NNPS and DQE fit well the experimental data.

We extracted the experimental input referred electrical signal ($d(\text{e}^-)$) at the sensing node by $d(\text{DN}) \times S(\text{e}^-/\text{DN})$. As shown in figure 6, the simulated $d(\text{e}^-)$, given by $(a_{pd})^2 \overline{q_0 g_1 g_2 g_4 g_6}$, is consistent with experimentally extracted data for K_a up to 127 μGy. Therefore, the gain parameters used in the simulation are validated. In addition, linear signal response is observed up to stage 6 of the cascaded system. The signal nonlinearity only occurs on the CMOS APS level (stage 9).

Figure 7 shows the measured and simulated mean output signal $d(\text{DN})$ and mean variance $\sigma^2(\text{DN}^2)$ at various x-ray exposure levels. In comparison to signal, remarkable mean variance nonlinearity over K_a is observed. This finding is consistent with the large variation in $N(\text{e}^-/\text{DN})$ as shown in figure 3. The mean signal and variance extracted experimentally and theoretically are consistent with each other. Hence, we demonstrated that the nonlinear compensation operated in cascaded system analysis is necessary and results in reliable analysis. The total system gain (G_{total}) of ~25 DN/μGy was extracted from the slope of $d(\text{DN})$ versus K_a curve.

3.2. Electrical properties of DynAMITe SP x-ray detector

In general, linear cascaded system analysis is applied to simulate the x-ray imaging performance of flat-panel x-ray detectors, while the electrical properties such as FW, DR and read noise of x-ray detectors are not evaluated. In this study, the nonlinear cascaded system analysis enables direct extraction of the electrical properties without additional optical or electrical measurements.

Figure 8 shows the total noise in RMS electrons ($\sigma(\text{e}^-)$) at K_a from 1 nGy to 1 mGy. $\sigma(\text{e}^-)$ is extracted by $\sigma(\text{DN}) \times K(\text{e}^-/\text{DN})$. At a very large K_a ($>285\ \mu$Gy), $\sigma(\text{DN})$ drops as $(g_{9,N}(\text{DN/e}^-))^2$ decreases fast with K_a. Here to extract the FW and DR, a constant conversion gain ($K = 0.024\ \text{e}^-/\text{DN}$) was used, so that $\sigma(\text{e}^-)$ is proportional to $\sigma(\text{DN})$.
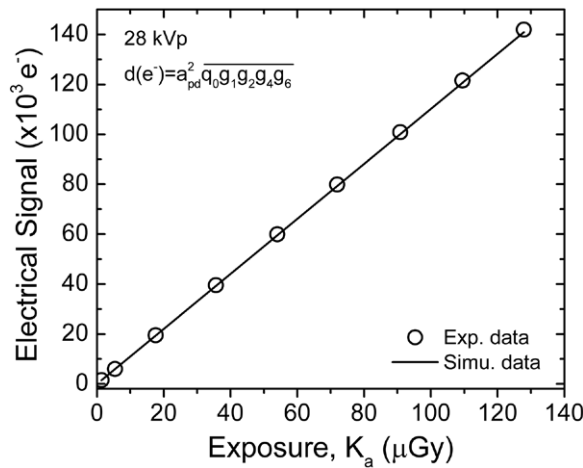
Figure 6. Experimental extracted (circles) and simulated (lines) electronic signal at the sensing node for detector air kerma up to 127 μGy.
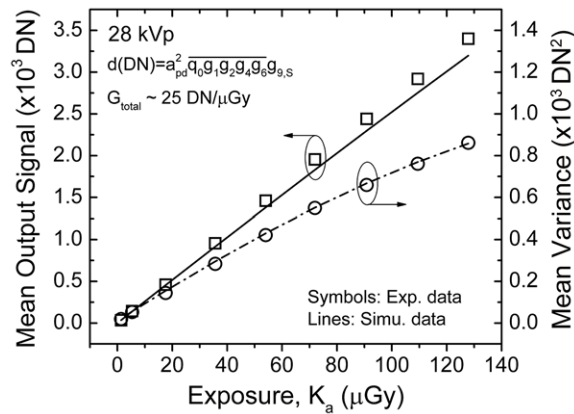

Figure 7. Experimental (symbols) and simulated mean output signal in DN and pixel mean variance in DN^2 for detector air kerma ranging from 1.3 to 127 μGy. Signal/noise non-linearity is included.

The full well capacity of a CMOS image sensor is given by $FW(e^-) = K(e^-/DN) \times d_{max}(DN) = d_{max}(e^-)$, where $d_{max}(e^-)$ is determined when $\sigma(DN)$ (i.e. $\sigma(e^-)$) reaches the maximum. At $K_{a,max} = 285$ μGy, $d_{max}(DN) = 6667$ DN, hence the FW of 2.8×10^5 e$^-$ was obtained.

The dynamic range is defined by the ratio of maximum ($K_{a,max}$) and minimum input signal ($K_{a,min}$). $K_{a,min}$ is normally defined when the SNR$_d$ reaches zero decibel, i.e. signal equal to noise. As shown in figure 8, the SNR$_d$ were calculated by equation (23) and we got $K_{a,min} = 0.14$ μGy. Thus $DR = 20 \log(K_{a,max}/K_{a,min}) = 66$ dB was extracted. Since the signal conversion from K_a to $d(e^-)$ is linear, the DR can also be calculated by $DR = 20 \log(FW(e^-)/\sigma_R(e^-)) = 66$ dB.

The electronic read noise ($\sigma_R \sim 145$ e$^-$) can be directly acquired from the noise floor at low exposure ($K_a < 0.1$ μGy) levels.
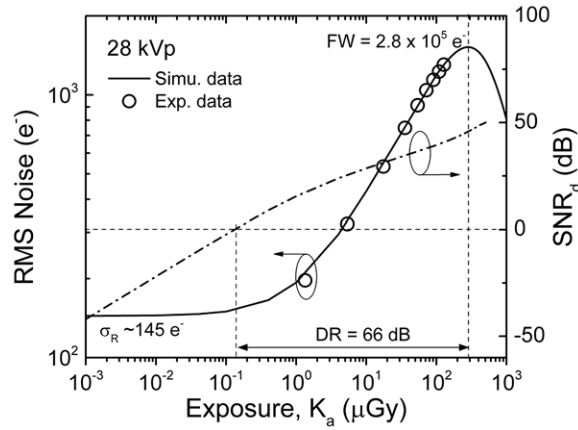
Figure 8. Experimental (circles) and simulated (solid line) RMS pixel total noise for DynAMITe SP detector at air kerma ranging from 10^{-3} to 10^3 μGy. The detector signal-to-noise ratio (SNR_d) (dash line) is also shown. Detector full well capacity (FW), read noise and dynamic range (DR) were extracted.

The extracted FW, DR and σ_R values from the nonlinear cascaded system analysis are consistent with the experimental and published results obtained by MV analysis (2.8×10^5 e^-, 66 dB, ~150 e^-, respectively) (Esposito *et al* 2011, 2014). Therefore, we demonstrated that the proposed cascaded system analysis in combination with signal/noise nonlinearity can be used as an efficient tool to evaluate the electrical properties of 50 μm pixel pitch CMOS APS x-ray detectors.

3.3. Temporal noise of DynAMITe SP x-ray detector

For low dose DBT application, when $K_a < 10$ μGy, the temporal noise (read noise) of CMOS APS x-ray imager can be the limiting factor for imaging performance. Thereby, to further improve the detector performance, the temporal noise of DynAMITe SP detector needs to be evaluated. In general, the total temporal noise of CMOS APS pixel circuit (σ_{pixel}) consists of reset noise (σ_{reset}), dark current shot noise (σ_{dark}), thermal noise for SF ($\sigma_{\text{th,SF}}$), RS ($\sigma_{\text{th,RS}}$) and Bias transistors ($\sigma_{\text{th,Bias}}$), and transistor flicker noise for RST ($\sigma_{\text{fl,RST}}$), SF ($\sigma_{\text{fl,SF}}$) and RS ($\sigma_{\text{fl,RS}}$):

$$\sigma_{\text{pixel}}^2 = \sigma_{\text{reset}}^2 + \sigma_{\text{dark}}^2 + \sigma_{\text{th,SF}}^2 + \sigma_{\text{th,RS}}^2 + \sigma_{\text{th,Bias}}^2 + \sigma_{\text{fl,RST}}^2 + \sigma_{\text{fl,SF}}^2 + \sigma_{\text{fl,RS}}^2 \tag{26}$$

where all the temporal noise components are in electrons and input referred to the sensing node.

The reset noise is described as

$$\sigma_{\text{reset}} = \sqrt{kTC_{\text{IN}}}/q \tag{27}$$

where k is the Boltzmann constant, T is the temperature, C_{IN} (~40 fF) is the total input capacitance.

The dark current shot noise is given by

$$\sigma_{\text{dark}} = \sqrt{J_{\text{dark}} a_{\text{pd}}^2 t_{\text{int}}/q} \tag{28}$$

where J_{dark} (~10 pA cm^{-2}) is the dark current density of c-Si photodiode, $(a_{pd})^2$ is the photodiode area, and t_{int} is the integration time (~0.15 s).

The thermal noise of SF, RS and Bias transistors was reported (Tian *et al* 2001). The input referred thermal noise for these transistors can be written as

$$\sigma_{th,SF} = \frac{C_{IN}}{qA_V}\left(\frac{2}{3}\frac{kT}{C_{Col}}\frac{1}{1+(g_{m,SF}/g_{d,RS})}\right)^{1/2} \tag{29}$$

$$\sigma_{th,RS} = \frac{C_{IN}}{qA_V}\left(\frac{kT}{C_{Col}}\frac{1}{g_{d,RS}(1/g_{d,RS}+1/g_{m,SF})}\right)^{1/2} \tag{30}$$

$$\sigma_{th,Bias} = \frac{C_{IN}}{qA_V}\left(\frac{kT}{C_{Col}}g_{m,Bias}\left(\frac{1}{g_{d,RS}}+\frac{1}{g_{m,SF}}\right)\right)^{1/2} \tag{31}$$

where A_V is the voltage gain (in V/V) of the SF (~0.8), C_{Col} is the transistor in the column line, $g_{m,SF}$, $g_{d,RS}$ and $g_{m,Bias}$ represent the transconductance of SF, channel conductance of RS and transconductance of Bias transistor, respectively.

The flicker noise ($\sigma_{fl,RST}$, $\sigma_{fl,SF}$ and $\sigma_{fl,RS}$) was calculated by adopting the non-stationary time domain model (Tian and El Gamal 2000):

$$\sigma_{fl,RST}^2 = \left(\frac{C_{IN}}{WLC_{ox}}\right)^2\frac{1}{(t_{rst}+\delta)^2}\int_0^{t_{rst}}\int_0^{t_{rst}}\int_{\lambda_L}^{\lambda_H}C_\lambda(t_1,|t_2-t_1|)g(\lambda)d\lambda dt_1 dt_2 \tag{32}$$

$$\sigma_{fl,SF}^2 = \left(\frac{g_{m,SF}C_{IN}}{A_V WLC_{ox}}\right)^2\frac{e^{-\frac{2g_{m,SF}}{C_{M2}}t_r}}{C_{M2}^2}\int_0^{t_r}\int_0^{t_r}\int_{\lambda_L}^{\lambda_H}C_\lambda(t_1,|t_2-t_1|)g(\lambda)e^{\frac{g_{m,SF}}{C_{M2}}(t_1+t_2)}d\lambda dt_1 dt_2 \tag{33}$$

$$\sigma_{fl,RS}^2 = \left(\frac{g_{m,RS}C_{IN}}{A_V WLC_{ox}}\right)^2\frac{e^{-\frac{2g_{d,RS}}{C_{M3}}t_r}}{C_{M3}^2}\int_0^{t_r}\int_0^{t_r}\int_{\lambda_L}^{\lambda_H}C_\lambda(t_1,|t_2-t_1|)g(\lambda)e^{\frac{g_{d,RS}}{C_{M3}}(t_1+t_2)}d\lambda dt_1 dt_2 \tag{34}$$

where W and L are the transistor channel width and length, C_{ox} is the gate oxide capacitance per unit area, t_{rst} is the reset time, t_r is the readout time, δ is the thermal time, λ stands for the transition rate for an electron to occupy a trap state, λ_H and λ_L are the highest and lowest transition rate respectively, $g_{m,RS}$ is the transconductance of RS, $C_{M2} = (1 + g_{m,SF}/g_{d,RS})C_{Col}$, $C_{M3} = (1 + g_{d,RS}/g_{m,SF})C_{Col}$, $C_\lambda(t,\tau)$ represents the auto-covariance function of the trap electron number $N(t)$, and $g(\lambda)$ is the distribution of λ, C_λ and $g(\lambda)$ are given by (Tian and El Gamal 2000)

$$C_\lambda(t,\tau) = \frac{1}{4}e^{-2\lambda\tau}(1-e^{-4\lambda t}) \tag{35}$$

$$g(\lambda) = \frac{4kTWLt_{ox}N_t}{\lambda\ln(\lambda_H/\lambda_L)} \tag{36}$$

where t_{ox} is the thickness of transistor gate oxide, N_t is the gate oxide trap density. Taking standard parameters for 0.35 μm CMOS technology, the flicker noise of RST, SF and RS were calculated.
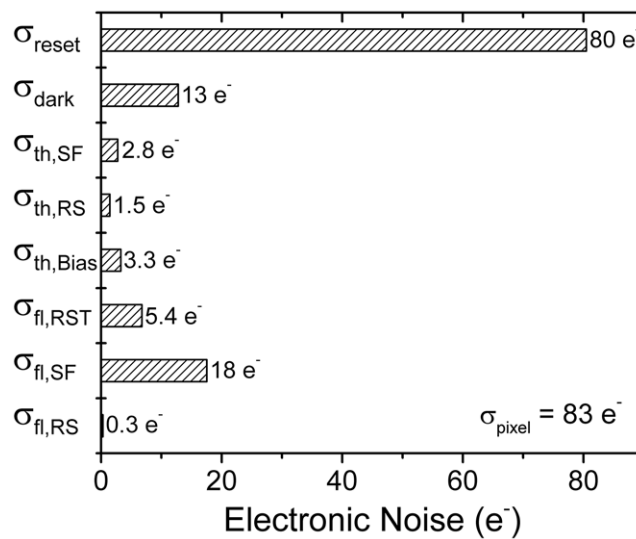
Figure 9. Calculated temporal noise of CMOS APS pixel and readout circuits.

All the temporal noise elements of CMOS APS pixel circuit are shown in figure 9. After adding up all the components, σ_{pixel} of 83 e$^-$ is obtained. The 50 μm pixel pitch CMOS APS pixel noise is mainly due to the reset kTC noise, σ_{reset} ~ 80 e$^-$, while dark current shot noise, thermal and flicker noise show negligible contributions to the total noise. The calculated σ_{pixel} deviates from the previously extracted read noise σ_R of ~145 e$^-$. The difference indicates the presence of a large readout circuit noise of >100 e$^-$ in the system. The FPN was removed by the image correction algorithm during the evaluation of imaging performance and excluded from the temporal noise analysis; hence it will not contribute to the extracted total read noise. Most likely, noise from external readout circuit electronics contributes the most to the extracted σ_R of ~145 e$^-$.

Assuming that in the future the external readout circuit noise can be reduced by better circuit design, the temporal noise is still limited by σ_{reset}. To minimize σ_{reset}, correlated double sampling (CDS) has been widely used in CMOS image sensor industry (El Gamal and Eltoukhy 2005, Lulé *et al* 2000). To realize real CDS, 4-T CMOS APS pixel design in combination with a pinned photodiode (PPD) is used (Burkey *et al* 1984, Guidash *et al* 1997). Within a single frame, CDS will read both a reset (dark) and an x-ray photon induced signal row by row (or column by column). The integration time of CDS with 4-T CMOS APS is determined by the time period between the PPD reset stage and carrier transfer stage in each row (or column), when the detector is irradiated (El Gamal and Eltoukhy 2005). Therefore, to implement such x-ray imaging technology, an extended (but not necessarily continuous) x-ray pulse width (including both the integration and readout times) is required, because the integration stage shifts during the readout process in each row (or column). A much lower σ_{read} of around 50–100 e$^-$ is expected using such technology. As discussed in section 3.4, this would help detect 100 μm microcalcifications. However, for such approach, an increased patient dose is expected. Additional studies are needed to explore the imager performance difference at the patient level, when the 4-T CMOS APS in combination with CDS is used.

Another approach to reduce noise is to reduce the pixel input capacitance (C_{IN}) by reducing the C_{PD} or C_{Par}. However, it would reduce d_{max}(e$^-$) and result in a small FW and DR. It is possible to address this issue by the novel pixel design introduced in DynAMITe x-ray

detector. For DBT application, when a low dose and a low noise are the major concern, the SP diode with a small C_{PD} (thus smaller C_{IN}) is activated. Therefore, the reset noise will be suppressed. At the same time, a large APS pixel conversion gain ($A_V \times q/C_{IN}$) would also minimize the dominant σ_{AMP} of the readout circuit. On the other hand, the P diode with a larger C_{PD} can be used for a large signal, when the read noise is insignificant in comparison to the quantum noise. Hence, by using dynamic switching between SP and P modes, both a low temporal noise and a large DR could be achieved at the same time, which was not included in the imager described in this work.

3.4. Image quality of microcalcifications

One of the major challenges for DBT is to be able to distinguish the microcalcifications within the breast tissue. Using the DynAMITe SP x-ray detector, we are interested in identifying microcalcifications with dimensions of 100 μm, which is Nyquist limit of 50 μm pixel pitch DynAMITe x-ray detectors. High resolution imagers can also provide microcalcification clusters shape and arrangement details that radiologists visually search for (Wheeler *et al* 2006). In this work, the breast image signal-to-noise ratio (SNR_i) is used to evaluate the image quality (image contrast) of microcalcifications in the breast tissue. Note that since no object contrast information is included, the SNR_d for a flat field image as discussed in section 3.2 only reflects the detector performance instead of DBT image quality.

Based on the Rose model, Burgess (1999) and Zhao *et al* (2005) reported that the object image SNR_i is given by

$$SNR_i = \sqrt{n} \cdot CNR \tag{37}$$

where

$$CNR = \frac{d_b - d_m}{\sigma_b} = \frac{d_b - d_m}{d_b} \cdot \frac{d_b}{\sigma_b} = C \cdot \frac{d_b}{\sigma_b} = C \cdot SNR_d \tag{38}$$

where n is the number of pixels fully covered by the object and CNR is the contrast-to-noise ratio of objects (Lu *et al* 2010, Park *et al* 2014). d_b and d_m are the pixel signal under the background (breast) and objects of interest (microcalcifications), respectively; σ_b is the standard deviation of the background signal; and C is the contrast of object given by $(d_b - d_m)/\sigma_b$. We have $n = 4$ and ~9 for microcalcifications with 100 and 165 μm diameters using the DynAMITe SP detector with a 50 μm pixel pitch.

A simulated x-ray spectrum at the breast skin surface for a combination of W anode and 0.7 mm Al filtration (28 kVp) (Boone and Seibert 1997, Boone 1998), referring to the clinical DBT system setup (Sechopoulos 2013), was used to calculate the contrast C. The contrast of microcalcification in a 1 mm slice of reconstructed DBT image was calculated using the method described in our previous work studying another CMOS APS x-ray detector (Dexela 2923 MAM) with 75 μm pixel pitch (Zhao *et al* 2015). The mass attenuation coefficients were obtained from Hubbel and Seltzer (1995). Breast densities of $0.93 - 1.04$ g cm^{-3} for glandular fraction from 0 to 100% and microcalcification density of ~1.54 g cm^{-3} were used in the calculation. The calculated C is around 0.215 and 0.320 for microcalcifications with size of 100 and 165 μm, respectively.

For clinical use, the relationship between calculated SNR_i and patient MGD needs to be extracted. The MGD was calculated using the method described by Sechopoulos *et al* (2007)

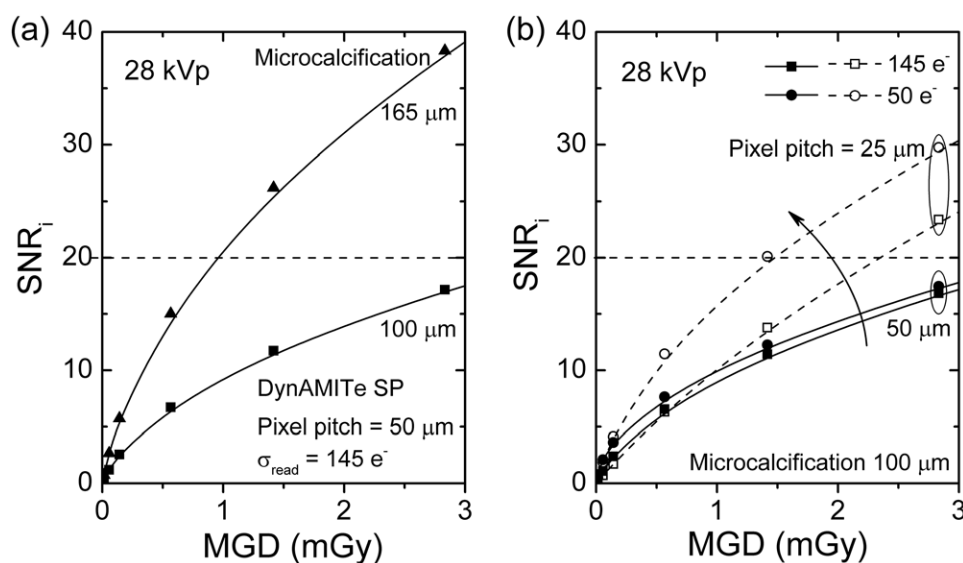$$MGD = X \cdot D_g N_0 \cdot \sum_\alpha RGD(\alpha) \tag{39}$$

Figure 10. Calculated detector SNR_i using MGD up to 3 mGy for (a) microcalcifications with sizes of 100 and 165 μm using the DynAMITe SP x-ray detector (pixel pitch of 50 μm and σ_{read} of 145 e$^-$) and (b) 100 μm microcalficiations using reduced pixel pitch of 25 μm and σ_{read} of 50 e$^-$.

where X is the breast skin exposure in Roentgen (R) for each projection, D_gN_0 is the normalized glandular dose in mGy/R for the zero degree projection (vertical to the detector), and $RGD(\alpha)$ is the relative glandular dose coefficient at each projection angle α.

We calculated X from the detector surface air kerma (Zhao *et al* 2015), D_gN_0 from the monoenergetic normalized glandular dose ($D_gN(E)$) with parameters tabulated by Boone (2002) and $RGD(\alpha)$ for a cranio-caudal (CC) view using the parameters provided by Sechopoulos *et al* (2007). For our calculation, a DBT scan angle of 15° ($\pm$7.5°) and a projection number of 15 was chosen to be consistent with a FDA approved Hologic Selenia Dimensions system (Sechopoulos 2013). An average breast with 5 cm thickness and 50% glandular fraction was considered in the calculation.

Figure 10(a) shows the calculated SNR_i at various MGD for microcalcifications with sizes of 100 and 165 μm using the DynAMITe SP x-ray detector. Park *et al* (2014) demonstrated that a threshold CNR of around 10 is required to clearly distinguish 165 μm microcalcifications using a CMOS APS x-ray detector with 75 μm pixel pitch (corresponding to $n \sim 4$ in equation (37)). Therefore, in this work, the threshold SNR_i for microcalcification identification is defined as 20. It can be seen that microcalcifications of 165 μm can be classified at MGD of 0.95 mGy. In comparison to the calculated MGD (~1.3 mGy for an average breast) using an amorphous selenium based PPS x-ray detector by Feng and Sechopoulos (2012), a 27% MGD reduction can be achieved. However, 100 μm microcalcifications cannot be detected using the current design of DynAMITe SP x-ray detector with 50 μm pixel pitch and σ_{read} of 145 e$^-$. Note that it is difficult to determine the correct threshold SNR_i without DBT image analysis. If the threshold SNR_i is 10, 100 μm microcalcifications can be detected at a MGD of around 1.1 mGy using the DynAMITe detector. Our SNR_i is theoretically calculated based on the Rose model. In practice, the detection limit for SNR_i should be evaluated for optimized x-ray beam quality, acquisition geometry and reconstruction algorithm in future work.

To distinguish microcalcifications of around 100 μm, complete DBT imaging system including CMOS APS detector, image acquisition and reconstruction must be optimized. For example,

the readout circuit could be optimized so that the readout electronics (>100 e$^-$) is suppressed; at the same time, 4-T CMOS APS pixel in combination with CDS could to be applied to reduce the reset noise (83 e$^-$). As the result, the total read noise σ_{read} can be reduced to around 50 e$^-$. As shown in figure 10(b), without changing the pixel pitch, SNR$_i$ for 100 μm microcalcifications using 50 μm CMOS APS x-ray detectors with σ_{read} of 50 e$^-$ shows a negligible improvement in comparison to DynAMITe SP x-ray detector ($\sigma_{read} = 145$ e$^-$). Next we reduced the pixel pitch to 25 μm, and used σ_{read} of 145 and 50 e$^-$ to calculate SNR$_i$. Note that SNR$_d$ was recalculated by cascaded system analysis for 25 μm pixel pitch, assuming all the other parameters were kept same. It is shown that at MGD of 1.5 mGy, 100 μm microcalcifications can be detected using a 25 μm pixel pitch CMOS APS x-ray detector with a 50 e$^-$ read noise. Hence, to further improve CMOS APS x-ray detectors for DBT, both the pixel pitch and the read noise reduction should be considered at the same time. The authors also tried to increase the *FF* to 0.9. However, the DQE, SNR$_d$ and SNR$_i$ increase (not shown) is negligible ($<5\%$). This increase will not have a major impact on 100 μm microcalcification detection. The limiting MGD for 100 μm microcalcification detection is around 1.5 mGy. To further reduce the MGD for DBT, low noise CMOS APS x-ray detector technology in combination with CDS and proper image acquisition geometry and new DBT dedicated image reconstruction techniques must be developed.

4. Conclusion

In this work, we measured the imaging performance such as MTF, NPS and DQE of a 50 μm pixel pitch wafer-scale CMOS APS x-ray detector. In comparison to conventional a-Si: H-based direct and indirect PPS x-ray detectors on the market, the spatial resolution is increased from around 5 to 10 mm^{-1} and a DQE > 0.5 is achieved at zero spatial frequency. The signal and noise nonlinearity of CMOS APS x-ray detector was studied and integrated into the cascaded system analysis. As the result, a nonlinear cascaded system model was developed for the 50 μm CMOS APS x-ray detector. Both the x-ray imaging and electrical properties of the DynAMITe SP x-ray detector were simulated with good agreements to experimental results. We found that the electrical noise of the DynAMITe SP x-ray detector is dominated by the reset noise and readout electronic noise. To improve the detector performance, these two noise sources have to be suppressed.

For the DBT application, the image quality of microcalcifications with sizes of 100 and 165 μm was measured by SNR$_i$. With a threshold SNR$_i$ of 20, it is possible to distinguish microcalcifications of 165 μm in size using the DynAMITe SP x-ray detector at a MGD of 0.95 mGy. To detect 100 μm microcalcifications using the CMOS APS detector; further optimization of the detector, acquisition geometry and image reconstruction should be considered.

Acknowledgments

References

Antonuk L E, Jee K-W, El-Mohri Y, Maolinbay M, Nassif S, Rong X, Zhao Q, Siewerdsen J H, Street R A and Shah K S 2000 Strategies to improve the signal and noise performance of active pixel, flat-panel imagers for diagnostic x-ray applications *Med. Phys.* **27** 289–306

Bissonnette M *et al* 2005 Digital breast tomosynthesis using an amorphous selenium flat panel detector *Proc. SPIE* **5745** 529–40

Bohndiek S E, Blue A, Clark A T, Prydderch M L, Turchetta R, Royle G J and Speller R D 2008 Comparison of methods for estimating the conversion gain of CMOS active pixel sensors *IEEE Sensors J.* **8** 1734–44

Bohndiek S E *et al* 2009 Characterization and testing of LAS: a prototype 'Large Area Sensor' with performance characteristics suitable for medical imaging applications *IEEE Trans. Nucl. Sci.* **56** 2938–46

Boone J M and Seibert A 1997 An accurate method for computer-generating tungsten anode x-ray spectra from 30 to 140 kV *Med. Phys.* **24** 1661–70

Boone J M 1998 Spectral modeling and compilation of quantum fluence in radiography and mammography *Proc. SPIE* **3336** 592–601

Boone J M 2002 Normalized glandular dose (D_gN) coeffcients for arbitrary x-ray spectra in mammography: computer-fit values of Monte Carlo derived data *Med. Phys.* **29** 869–75

Burgess A E 1999 The rose model, revisited *J. Opt. Soc. Am.* A **16** 633–46

Burkey B C, Chang W C, Littlehale J, Lee T H, Tredwell T J, Lavine J P and Trabka E A 1984 The pinned photodiode for an interline-transfer CCD image sensor *IEDM'84: Int. Electron Devices Meeting* pp 28–31

Cha B K, Bae J H, Kim B-J, Jeon H, and Cho C 2008 Performance studies of a monolithic scintillator-CMOS image sensor for x-ray application *Nucl. Instrum. Methods Phys. Res.* A **591** 113–6

Choi J G, Park H S, Kim Y S, Choi Y W, Ham T H and Kim H J 2012 Characterization of prototype full-field breast tomosynthesis by using a CMOS array coupled with a columnar CsI(Tl) scintillator *J. Korean Phys. Soc.* **60** 521–6

Cunningham I A 1997 Degradation of the detective quantum efficiency due to a non-unity detector fill factor *Proc. SPIE* **3032** 22–31

Cunningham I A and Shaw R 1999 Signal-to-noise optimization of medical imaging systems *J. Opt. Soc. Am.* A **16** 621–32

Eid E, Chan T Y, Fossum E R, Tsai R H, Spagnuolo R, Deily J, Byers W B and Peden J C 2001 Design and characterization of ionizing radiation-tolerant CMOS APS image sensors up to 30 Mrd (Si) total dose *IEEE Trans. Nucl. Sci.* **48** 1796–806

El Gamal A and Eltoukhy H 2005 CMOS image sensors *IEEE Circuit Device Mag.* **21** 6–20

El-Mohri Y, Antonuk L E, Zhao Q, Wang Y, Li Y, Du H and Sawant A 2007 Performance of a high fill factor, indirect detection prototype flat-panel imager for mammography *Med. Phys.* **34** 315–27

Esposito M, Anaxagoras T, Fant A, Wells K, Konstantinidis A C, Osmond J P F, Evans P M, Speller R D and Allinson N M 2011 DynAMITe: a wafer scale sensor for biomedical applications *J. Inst.* **6** C12064

Esposito M, Anaxagoras T, Diaz O, Wells K and Allinson N M 2012 Radiation hardness of a large area CMOS active pixel sensor for bio-medical applications *NSS/MIC'12: IEEE Nuclear Science Symp. and Medical Imaging Conf.* pp 1300–4

Esposito M, Anaxagoras T, Konstantinidis A C, Zheng Y, Speller R D, Evans P M, Allinson N M and Wells K 2014 Performance of a novel wafer scale CMOS active pixel sensor for bio-medical imaging *Phys. Med. Biol.* **59** 3533–54

Feng S S J and Sechopoulos I 2012 Clinical digital breast tomosynthesis system: dosimetric characterization *Radiology* **263** 35–42

Fossum E R 1995 CMOS image sensors: electronic camera on a chip *IEDM'95: Int. Electron Devices Meeting* pp 17–25

Guidash R M, Lee T H, Lee P P K, Sackett D H, Drowley C I, Swensen M S, Arbaugh L, Hollstein R, Shapiro F and Domer S 1997 A 0.6 μm CMOS pinned photodiode color imager technology *IEDM'97: Int. Electron Devices Meeting* pp 927–9

Hejazi S and Trauernchit D P 1997 System considerations in CCD-based x-ray imaging for digital chest radiography and digital mammography *Med. Phys.* **24** 287–97

Hillen W, Eckenbach W, Quadflieg Q and Zaengel T 1991 Signal-to-noise performance in cesium iodide x-ray fluorescent screens *Proc. SPIE* **1443** 120–31

Holl I, Lorenz E and Mageras G 1988 A measurement of light yield of common inorganic scintillators *IEEE Trans. Nucl. Sci.* **35** 105–9

Hubbel J H and Seltzer S M 1995 Table of x-ray mass attenuation coefficient and mass energy-absorption coefficient 1 keV to 20 MeV for elements $Z = 1$ to 92 and 48 additional substances of dosimetric interest *NISTIR Report* 5632 (Gaithersburg, MD: NIST) (www.osti.gov/scitech/biblio/76335)

IEC 62220-1-2 2007 *Medical Electrical Equipment—Characteristics of Digital X-Ray Imaging Devices—Part 1-2: Determination of the Detective Quantum Efficiency—Detectors Used in Mammography* (Geneva: International Electrotechnical Commission) (https://webstore.iec.ch/publication/6598)

Jain A, Bednarek D R, Ionita C and Rudin S 2011 A theoretical and experimental evaluation of the microangiographic fluoroscope: a high-resolution region-of-interest x-ray imager *Med. Phys.* **38** 4112–26

Janesick J, Pinter J, Potter R, Elliott T, Andrews J, Tower J, Cheng J and Bishop J 2009 Fundamental performance differences between CMOS and CCD imagers: part III *Proc. SPIE* **7439** 743907

Konstantinidis A C 2011 Evaluation of digital x-ray detectors for medical imaging applications *PhD Thesis* University College London (http://discovery.ucl.ac.uk/id/eprint/1322919)

Konstantinidis A C, Szafraniec M B, Speller R D and Olivo A 2012a The Dexela 2923 CMOS X-ray detector: a flat panel detector based on CMOS active pixel sensors for medical imaging applications *Nucl. Instrum. Methods Phys. Res.* A **689** 12–21

Konstantinidis A C, Zheng Y, Olivo A, Bliznakova K, Yip M, Anaxagoras T, Wells K, Allinson N and Speller R D 2012b Evaluation of a novel wafer-scale CMOS APS x-ray detector for use in mammography *NSS/MIC'12: IEEE Nuclear Science Symp. and Medical Imaging Conf.* pp 3254–60

Konstantinidis A, Anaxagoras T, Esposito M, Allinson N and Speller R D 2012c DynAMITe: a prototype large area CMOS APS for breast cancer diagnosis using x-ray diffraction measurements *Proc. SPIE* **8313** 83135H

Konstantinidis A C *et al* 2013 X-ray performance evaluation of the Dexela CMOS APS x-ray detector using monochromatic synchrotron radiation in the mammographic energy range *IEEE Trans. Nucl. Sci.* **60** 3969–80

Lacoe R C 2008 Improving integrated circuit performance through the application of hardness-by-design methodology *IEEE Trans. Nucl. Sci.* **55** 1903–25

Lu Y, Chan H-P, Wei J and Hadjiiski L M 2010 Selective-diffusion regularization for enhancement of microcalcifications in digital breast tomosynthesis reconstruction *Med. Phys.* **37** 6003–14

Lulé T, Benthien S, Keller H, Mütze F, Rieve P, Seibel K, Sommer M and Böhm M 2000 Sensitivity of CMOS based imagers and scaling perspectives *IEEE Trans. Electron Devices* **47** 2110–22

Naday S, Bullard E F, Gunn S, Brodrick J E, O'Tuairisg E O, McArthur A, Amin H, Williams M B, Judy P G and Konstantinidis A 2010 Optimised breast tomosynthesis with a novel CMOS flat panel detector *Digital Mammography* (Berlin: Springer) pp 428–35

Nikl M 2006 Scintillator detectors for x-rays *Meas. Sci. Technol.* **17** R37–54

Pain B and Hancock B J 2003 Accurate estimation of conversion gain and quantum efficiency in CMOS imagers *Proc. SPIE* **5017** 94–103

Park H S, Kim Y S, Kim H J, Choi Y W and Choi J G 2014 Optimization of configuration parameters in a newly developed digital breast tomosynthesis system *J. Radiat. Res.* **55** 589–99

Patel T, Klanian K, Gong Z and Williams M B 2012 Detective quantum efficiency of CsI-CMOS x-ray detector for digital breast tomosynthesis operating in high dynamic range and high sensitivity modes *Breast Imaging* (Lecture Notes in Computer Science vol 7361) (Berlin: Springer) pp 80–7

Salama K and El Gamal A 2003 Analysis of active pixel sensor readout circuit *IEEE Trans. Circuits Syst.* I **50** 941–5

Samei E, Flynn M J and Reimann D A 1998 A method for measuring the presampled MTF of digital radiographic systems using an edge test device *Med. Phys.* **25** 102–13

Scheffer D 2007 A wafer scale active pixel CMOS image sensor for generic x-ray radiology *Proc. SPIE* **6510** 65100O

Sechopoulos I, Suryanarayanan S, Vedantham S, D'Orsi C and Karellas A 2007 Computation of the glandular radiation dose in digital tomosynthesis of the breast *Med. Phys.* **34** 221–32

Sechopoulos I 2013 A review of breast tomosynthesis. Part I. The image acquisition process *Med. Phys.* **40** 014301

Sharma D, Badal A and Badano A 2012 hybridMANTIS: a CPU-GPU Monte Carlo method for modeling indirect x-ray detectors with columnar scintillator *Phys. Med. Biol.* **57** 2357–72

Siewerdsen J H, Antonuk L E, El-Mohri Y, Yorkston J, Huang W, Boudry J M and Cunningham I A 1997 Empirical and theoretical investigation of the noise performance of indirect detection, active pixel flat-panel imagers (AMFPIs) for diagnostic radiology *Med. Phys.* **24** 71–89

Siewerdsen J H, Waese A M, Moseley D J, Richard S and Jaffray D A 2004 Spektr: a computational tool for x-ray spectral analysis and imaging system optimization *Med. Phys.* **31** 3057–67

Tian H and El Gamal A 2000 Analysis of 1/*f* noise in CMOS APS *Proc. SPIE* **3965** 168

Tian H, Fowler B and El Gamal A 2001 Analysis of temporal noise in CMOS photodiode active pixel sensor *IEEE J. Solid-State Circuits* **36** 92–101

Tward D J and Siewerdsen J H 2008 Cascaded system analysis of the 3D noise transfer characteristics of flat-panel cone-beam CT *Med. Phys.* **35** 5510–29

Van Metter R L, Beutel J and Kundel H L 2000 *Handbook of Medical Imaging: Physics and Psychophysics* vol 1 (Bellingham, WA: SPIE) pp 37–69

Vedantham S, Karellas A and Suryanarayanan S 2004 Solid-state fluoroscopic imager for high-resolution angiography: Parallel-cascaded linear system analysis *Med. Phys.* **31** 1258–68

Wheeler F W, Amitha Perera A G, Claus B E, Muller S L, Peters G and Kaufhold J P 2006 Microcalcification detection in digital tomosynthesis mammography *Proc. SPIE* **6144** 614420

Yadid-Pecht O and Etienne-Cummings R 2004 *CMOS Imagers: from Phototransduction to Image Processing* (Norwell, MA: Kluwer) pp 99–139

Zentai G 2011 Comparison of CMOS and a-Si flat panel imagers for x-ray imaging *IST'11: Int. Conf. Imaging Systems and Techniques* pp 194–200

Zhao B and Zhao W 2008 Imaging performance of an amorphous selenium digital mammography in a breast tomosynthesis system *Med. Phys.* **35** 1978–87

Zhao C, Konstantinidis A C, Patel T and Kanicki J 2015 Large area CMOS active pixel sensor x-ray imager for low dose digital breast tomosynthesis: analysis, modeling and characterization *Med. Phys.* **42** 6294–308

Zhao W, Deych R and Dolazza E 2005 Optimization of operational conditions for direct digital mammography detectors for digital tomosynthesis *Proc. SPIE* **5745** 1272–81

Zhao W, Ristic G and Rowlands J A 2004 X-ray imaging performance of structured cesium iodide scintillators *Med. Phys.* **31** 2594–605